## Subproject A4.2

# Nanostructured organic photodiodes

**Principal Investigators: Uli Lemmer, Hans-Jürgen Eisler**

**CFN-Financed Scientists: Sebastian Valouch, Klaus Huska**

**Further Scientists: Dr. Jurana Hetterich, Dr. Alexander Colsmann, Carola Moosmann, Katja Dopf, Matthias Wissert, Siegfried Kettlitz, Nico Christ**

**Funding: One Ph.D. position since October 2007**

**Lichttechnisches Institut**
**Karlsruher Institut für Technologie (KIT)**

# Nanostructured organic photodiodes

## Introduction

Optoelectronic devices based on organic semiconductors are attracting more and more interest for a variety of applications. One of the most prominent applications is the use of organic light-emitting diodes (OLEDs) in passive matrix displays as used in mobile phones and MP3-audio players [1, 2].

For large-area, low-cost applications organic solar cells and photodetectors are of great interest [3, 4, 5, 6], as organic devices can be fabricated by low-cost manufacturing methods both based on evaporation or printing and coating on a wide range of different substrates [7]. These include not only traditional substrates for electronics such as silicon or glass but also metal foils or even polymers and paper [8]. It is therefore possible to find new applications that can not be addressed by traditional inorganic semiconductors. An obvious and very promising example are organic solar cells on flexible plastic substrates, as already being commercialized by the start-up company Konarka. But polymer substrates are not only interesting for large-area applications, they can also serve as the basis for integrated optical systems such as lab-on-a-chip systems [9, 10, 11, 12, 13]. Also, the fact that organic semiconductors can be easily patterned opens up new applications in the field of microoptics [A4.2:3, 14].

Organic photodiodes have been in the focus of subproject A4.2.The combination of organic photodiodes with micro- and nanostructures is promising, as the comparably easy production steps necessary to manufacture these devices can be nicely combined with nanopatterning processes. In comparision to conventional inorganic semiconductor devices, interface effects (such as nonradiative recombination and carrier trapping) are not as pronounced.
In addition, the organic photodiode is a nanotechnology research object itself since the device operation relies on a nanocomposite system such as the bulk heterojunction formed by a conjugated polymer and a functionalized fullerene.

As a particularly interesting feature, such organic semiconductor devices can be easily combined with plasmonic nanostructures, for example via nanoantennas. Nanoantennas are the scaled down version of conventional radio wave antennas with feature sizes as small as 20 nm, resonant at visible wavelengths. Metallic nanostructures are designed to efficiently convert free-space radiation from an area larger than their physical dimensions to a localized strongly enhanced field in a confined sub-wavelength dimension by supporting highly efficient localized surface plasmon resonances. Due to their high quantum efficiencies in emission and detection, organic devices combined with plasmonic nanostructures are very promising for future single photon organic devices. Our subproject aims at an understanding of the fundamental limitations of nanoscale organic optoelectronic devices and at the realization nanoantenna devices comprising active organic semiconductors.

## 1. Materials

The typical configuration of an organic photodiode is composed of four key parts: a substrate, an electrode, an active organic layer and a counter electrode on top as depicted in Fig. 1.

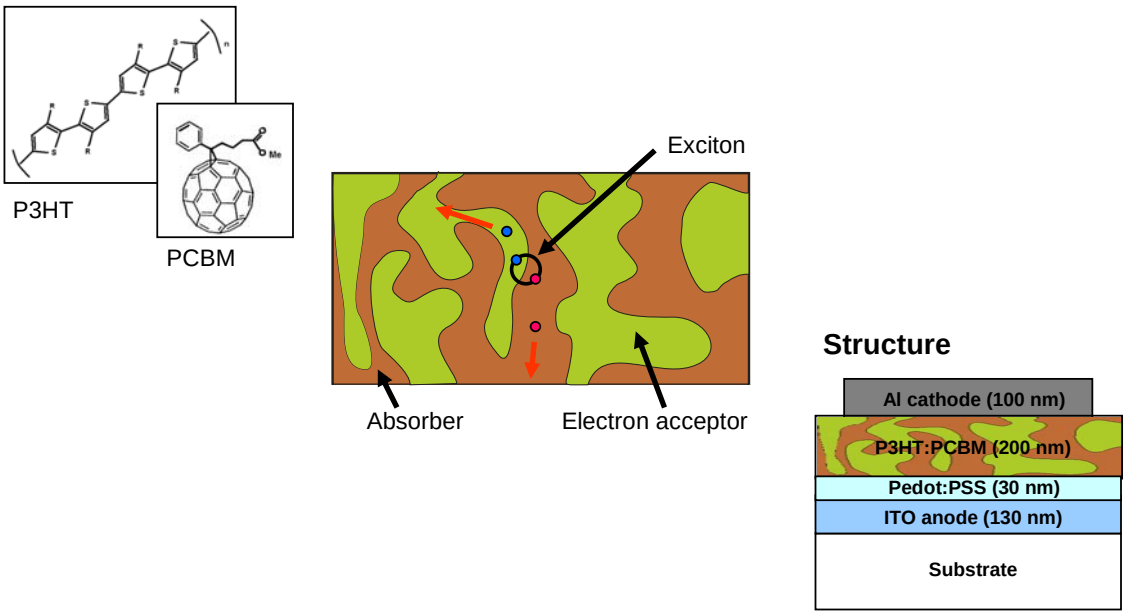


Fig. 1: Typical layer stack of a solution processed organic photodiode. Here the organic semiconductor PEDOT:PSS is used as hole injection layer and a blend of P3HT and PCBM forms the active layer of the device. Layer thicknesses are on the order of a few 10 nm.

Optical sensor systems as well as data transmission systems comprising organic photodiodes (OPDs) have been demonstrated [A4.2:3, 18, 19]. Here, both a high sensitivity and a fast photoresponse to light pulses are needed. Both classes of materials, conjugated polymers as well as evaporated small molecules, have been used for the fabrication of OPDs in the past [20, 21]. Multiheterostructure photodetectors based on small molecules with high efficiencies and fast response times have been demonstrated [21, 22]. While evaporation allows the creation of highly efficient and fast devices, an even easier way is the use of nanocomposite bulk heterojunctions which can be solution processed from a common solvent [23]. The interpenetrating network exhibits a high absorption of photons [25] and a highly effective generation and subsequent dissociation of excitons at the interface between the two materials. The exciton dissociation process can be as fast as 45 fs [24].

One of the most widely studied material combination for organic bulk heterojunctions is a blend of poly(3-hexylthiophene-2,5-diyl) (P3HT), a polythiophene derivative, and [6,6]-phenyl-$C_{61}$-butyric acid methyl ester (PCBM), a fullerene derivative. It shows a high mobility for charge carriers, an absorption ranging up to a wavelength of 650 nm and a high external quantum efficiency when used as the active layer of organic solar cells [25, 26, 27, 28, 29]. However, for the application in photodiodes other parameters are of interest than in solar cells. These are for example a low dark current, a high on-off ratio, a fast response and a spectral response that matches the rest of the system. Our project has focused on a deeper understanding and an optimization of these aspects.

## 2. High-speed organic photodiodes

To determine the basic properties and the dynamic photocurrent response of organic photodetectors based on P3HT:PCBM we fabricated devices utilizing a special high-frequency coaxial contact layout. A schematic view of the investigated organic photodetectors and the elaborated geometry is shown in Fig. 2. Device layout and contacts are optimized for high-frequency operation. Path lengths of the electrodes are minimized and parasitic capacitances formed by overlapping electrodes are avoided. Thus, *RC* time constants of the devices are not the limiting factor in their dynamic response. They were analyzed under continuous wave and pulsed laser illumination (532 nm). The organic photodiodes exhibit a pulse response with a full width at half maximum of 11 ns to the applied 1.6-ns-long laser pulses. Rise times as small as 1.6 ns and fall times of 40 ns were measured under applied reverse bias.

### 2.1 Fabrication

The devices are fabricated on glass substrates coated with an indium tin oxide layer (thickness of 120 nm) as the transparent electrode (Merck; sheet resistance of 20 Ω/sq). The substrate is treated by an oxygen plasma in order to improve the wetting ability in the following spin coating deposition of the hole transport layer poly(3,4-ethylenedioxythiophene):poly(styrenesulfonate) (PEDOT:PSS; H.C. Starck; mixed 1:1 with de-ionized water; ultrasonic treatment for 10 min; thickness of 40 nm). All active layers are deposited under nitrogen atmosphere in a glovebox. The remaining water contents are evaporated in a vacuum oven at 120 °C for 30 min. The active materials P3HT and PCBM (purchased from Rieke Metals and Solenne BV) are mixed in a 1:1 weight ratio, solved in 1,2-dichlorobenzene, and spin coated (thickness of 170 nm). Aluminum electrodes with a circular diameter of 500 µm (thickness of 340 nm) are thermally evaporated onto the active layers in a high vacuum chamber (Lesker Spectros; $3x10^{-7}$ mbar) through a laser-written shadow mask.

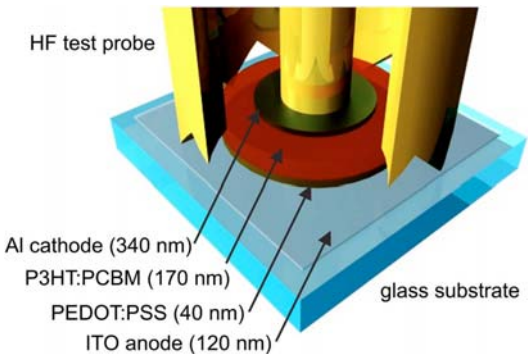


Fig. 2: Schematic device structure of the P3HT:PCBM bulk heterojunction photodetector (not to scale). The radiation sensitive area is defined by the structured Al cathode. A high frequency testprobe is employed for contacting. Light is incident from the bottom [A4.2:2].

### 2.2 Characterization

The characterization of the devices was done in a computerized optical setup utilizing a passively Q-switched frequency-doubled Nd:YAG laser as pulsed light source and a frequency-doubled Nd:$YVO_4$ laser as cw source, both at a wavelength of 532 nm. The light beams were attenuated with several absorption filters to obtain the desired intensity level.

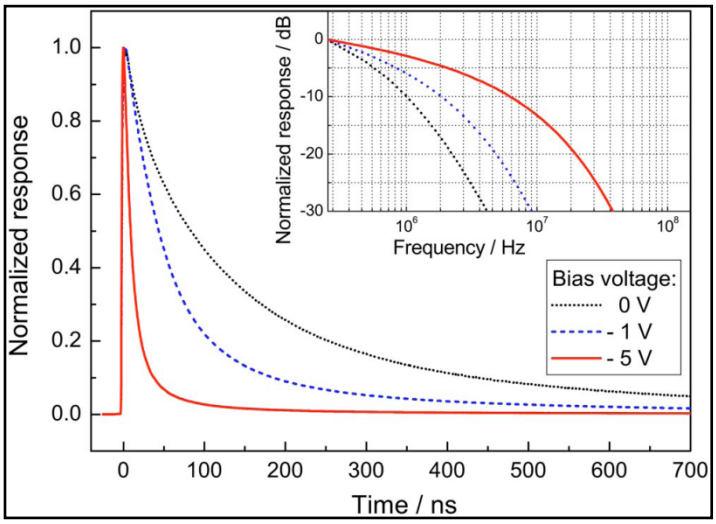


Fig. 3: Bias-dependent normalized pulse response of a 500 µm diameter photodetector following a 1.6 ns laser pulse @ 532 nm; average pulsed irradiance of 12 mW/cm². FWHM of the −5 V biased device: 11 ns. Inset: fast Fourier transformation of the pulse response. The −3 dB bandwidth at −5 V bias is ~1 MHz.

The results of the dynamic characterization under pulsed illumination are shown in Figs. 3 and 4. For better comparison between the curves, the bias-dependent photoresponse is normalized in Fig. 3. The dependence of the photoresponse amplitude and speed with different applied bias voltages is depicted. The device exhibits a near linear behavior in dependence of the bias in this voltage range. The OPD displays a fast pulse response with short rise times and longer fall times. Rise times are as low as 1.6 ns at −5 V bias. The fall times are strongly dependent on the applied bias voltage. The charge carriers are swept out of the device at increasing speed with an increasing electric field. The fall times (90%– 10%) show a significant decrease from 426 ns to 36 ns at 0 and −5 V bias, respectively.

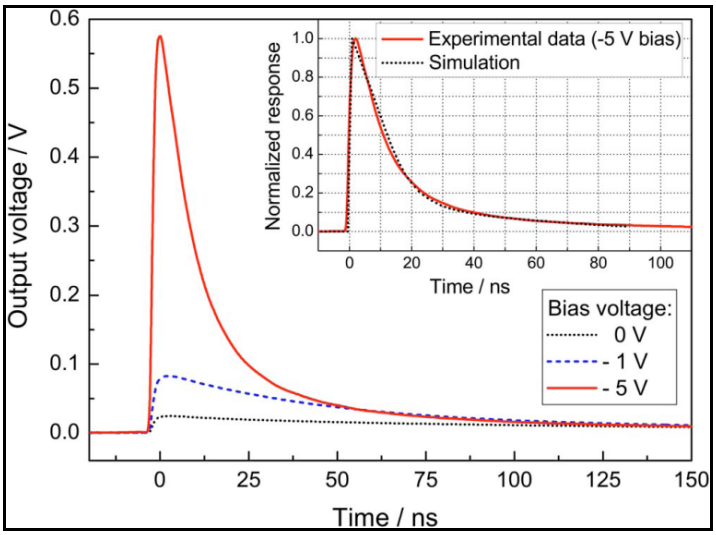


Fig. 4: Bias-dependent pulse response of a 500 µm diameter organic photodetector following a 1.6 ns laser pulse @ 532 nm; average pulsed irradiance of 12 mW/cm². Inset: comparison between experimental data and simulation at −5 V bias.

From the fast Fourier transformation (FFT) of the impulse response (see inset of Fig. 3), we derive a −3 dB cutoff frequency of ~1 MHz at −5 V bias. Also, considering the short full width at half maximum (FWHM) (11 ns) of the devices this clearly shows the applicability of these photodetectors for high speed applications. Nevertheless, the frequency response is strongly influenced by the slow tail of the photoresponse as this prohibits a flat response in the lower frequency regime of the FFT plot. For a deeper understanding of the origin of the slow tail, we have extended an existing drift/diffusion model for organic optoelectronic devices [30, 31, 32].

First simulation results show that the drifting photo generated charge carriers are causing space charge effects reducing the electric field strength, as the charge carriers a drifting in opposite direction. This field reduction reduces the drift velocity of the charge carriers, which can be the main cause of the slow tail, depending on the laser intensity. In the inset in Fig. 4 good agreement between simulated and experimental data for a bias voltage of −5 V is shown. When calculating the EQE of the device under pulsed irradiation (using the incident photon flux and the integrated pulse response) a value of 34% at −5 V bias is evaluated. This is in agreement with the value derived under cw illumination (36%) and indicates that the same mechanisms are operative. We deduce a responsivity of 0.15 A/W at 532 nm. This value is of the same order as commercially available silicon photodiodes. In conclusion, we have fabricated and characterized organic nanocomposite photodetectors. The devices feature high efficiencies and a fast photoresponse comparable with inorganic Si photodiodes.
In order to improve the spectral range of organic photodiodes, we incorporate PbS quantum dots into P3HT:PCBM devices. These quantum dot enhanced devices show a sensitivity not only in the spectral range of P3HT, but also in the infrared region which greatly expands the applicability of solution processed organic photodetectors [A4.2:5].

### 2.3 Simulation of the optoelectronic properties

Based on the first promising results the simulation work was further intensified. In addition to the transport processes also relevant for light emitting devices, we have included an optical model for the calculation of the spatially dependent generation rate. The optical model is based on a Transfer-Matrix-approach [A4.2:6], taking into account interference effects.

As mentioned in Section 2.2, space charge effects are one cause for the slow tail of the photoresponse. Besides that, depending on the device size (diameter of the OPD) and the laser intensity, the voltage drop at an external resistance causes a displacement current, as the change in the voltage drop can be high at the raising edge of the current density. As the comparison of experimental results and simulations for different device diameters demonstrates, it is very important to account for this effect in the simulation of the transient current density, too [A4.2:6]. Besides a prolonged photoresponse for larger device diameters, the time of the maximum is also shifted to later times due to the influence of the external resistance, as shown in Fig. 5.

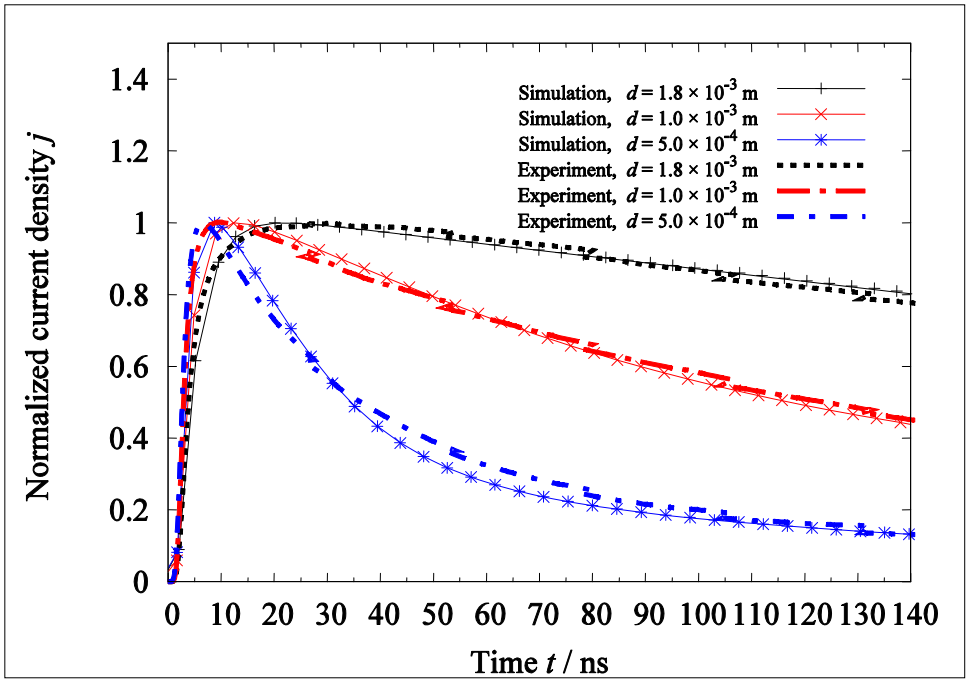


Fig. 5: Comparison of the measured and simulated photoresponse for different device diameters [A4.2:6]

The measured photoresponses show a strong dependence on the laser intensity, which is varied from P = 4.63 x $10^4$ W/m² up to P = 7.67 x $10^6$ W/m² in the measurements. Both the raise and the fall time are changing for several nanoseconds, as space charge effects are highly dependent on density of generated charge carriers. The higher the laser intensity, the stronger the drop in the electric field around the local maxima of the generated charge carriers, drifting in opposite direction. Furthermore the higher current density is causing a higher voltage drop at the external resistance, slowing down as well the tail of the photoresponse for higher laser intensities [A4.2:6].
In addition, our simulation reproduces very well the electric field dependence of the transient photoresponse for different applied voltages. The higher the applied voltage, the faster the charge carriers are extracted in the increased electric field.
From the detailed modelling of the pulse response for different laser intensities, different applied voltages and different device diameters in comparison with experimental results, we can determine a single set of parameters. It turns out that the first part of the decay curve is most sensitive to the electron mobility, while the tail of the signal depends critically on the hole mobility. The electron mobility is estimated to be $\mu_e$=3.5x$10^{-7}$ $m^2$ $V^{-1}$ $s^{-1}$ and the hole mobility $\mu_h$=3x$10^{-8}$ $m^2$ $V^{-1}$ $s^{-1}$.

With our approach, we are able to distinguish the influence of different physical effects as they become dominant at different current densities or in different time regimes. As mentioned above, this is in particular applicable on the charge carrier transport of electrons and holes. Temperature dependent measurements can give us detailed information about charge carrier transport phenomena as well as charge carrier generation and recombination processes. We performed measurements for a temperature range from T=10° C to T=50° C, as shown in Fig. 6. The pulse maximum considerably increases with higher temperature, while at the same time the decline of the current density after the maximum becomes faster. As described in more detail in [A4.2:9], we can attribute this to an enhanced mobility of the charge carriers. A suitable model to describe charge carrier transport in disordered materials is the Correlated Disorder Model (CDM), which we used to model the temperature dependent measurements. By fitting the experimental results we can deduce a rise

of 90% of the electron mobility, which is a rather big chance considering the relatively small temperature variation, indicating the importance of taking temperature effects into account.

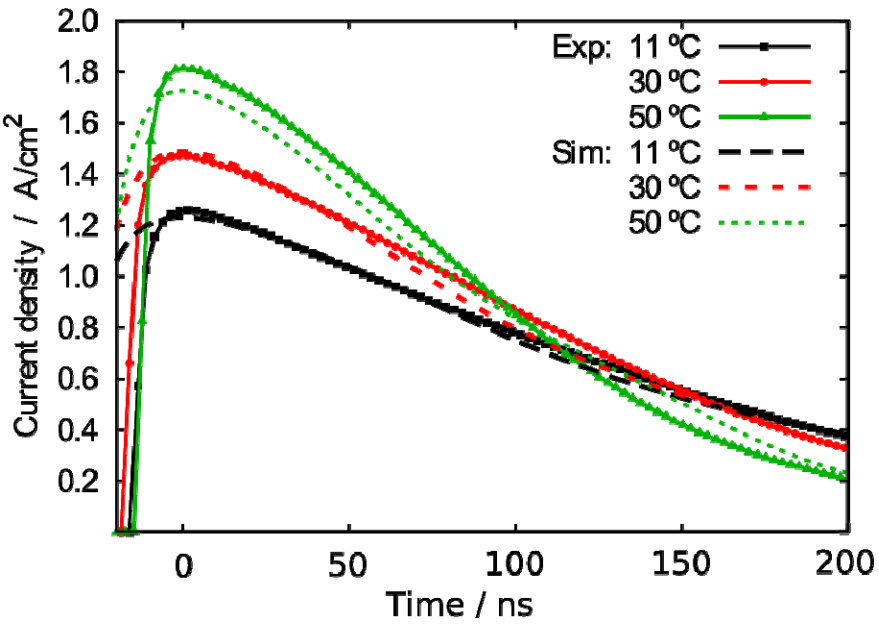


Fig. 6: Measured and simulated pulse responses at different temperatures. The laser power density is 6.7 x $10^6$ W/m2 and the bias voltage −3 V. The Correlated Disorder Model is used to describe the mobilities. [A4.2:9]

### 3. Optical Interconnects based on nanopatterned organic optoelectronic devices

Optical interconnects are one of the future interconnect technologies for future photonic communication on the chip- and PCB-level [33, 34, 35, 36, 37]. Based on the successful fabrication of high-speed organic photodetectors we were able to use OPDs and OLEDs together as optoelectronic components in a digital-audio optical interconnect [A4.2:4]. Our optical interconnect system is designed to achieve a data transfer rate that suits the digital S/PDIF standard. This standard is commonly used in consumer and semi-professional HiFi applications for interconnection between high quality audio components. We use a stereo audio source with a 44.1 kHz sampling rate which corresponds to a bit rate of 2.8224 Mbit/s. The data is encoded according to the biphase-mark-code (BMC) which inherently provides a good basis for synchronization and clock recovery. The resulting encoded transmission signal comprises pulses with a length of 177.2 and 354.3 ns. We employ a commercially available polymer optical fibre (POF) along with the optical fibre connection system TOSLINK [38], which is a common standard for the interconnection of audio components. The optical fibre is butt-coupled to the glass substrate of the OLED and OPD. The transmitter and receiver are designed for minimum response times, high efficiency, and optimum coupling to the fibre. The maximum spectral output at 520 nm of the OLED matches both a region of low attenuation in the POF and a maximum of absorption and quantum efficiency of the organic photodiode.

A crucial part of an all-organic optical interconnect is a fast and highly efficient OLED as the transmitter and a sensitive and fast photodiode. Fig. 7 shows the schemes of the devices. We employ a small molecule double heterostructure OLED with a fluorescent emitter ($Alq_3$) ensuring a fast dynamic response. A photolithographically structured SU-8 layer (5 µm thickness) is used to

define the active area of the OLED. As a receiver for the optical interconnect we investigate OPDs based on the concept of a bulk heterojunction. The absorption of the P3HT:PCBM with an absorption peak at ~500 nm matches the $Alq_3$-OLED emission perfectly. All devices were built on ITO glass with a reduced thickness (PGO; substrate thickness 400 µm; ITO sheet resistance ~15 Ω/sq) to reduce coupling losses.

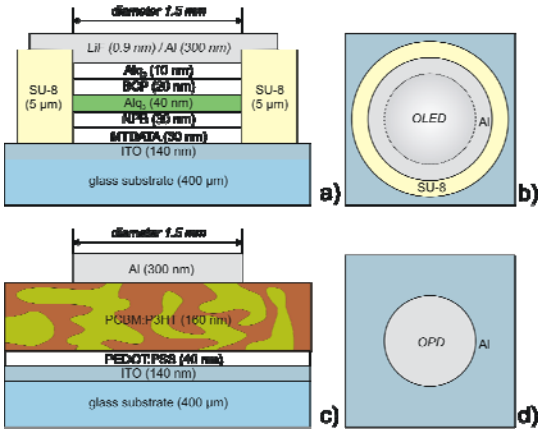


Fig. 7: (a) Layer structure of the $Alq_3$-OLED. (b) The materials are deposited by thermal evaporation. The active area of the OLED is defined by a structured SU-8 insulation layer as shown in the top view. (c) Layer structure of the P3HT:PCBM-OPD. (d) The materials are deposited by spincoating except the aluminium cathode, which is thermally evaporated. The active area is defined by the top electrode.

Because of the high device capacitance, it is not possible to achieve the necessary OLED bandwidth at the 50 Ω output impedance of a standard function generator. Even small area devices can have a capacitance reaching several nF which results in rise and fall times of tens of nanoseconds due to the low-pass behavior of the resulting RC circuit. We therefore use a MOSFET gate driver IC (IXYSRF DEIC420) designed for driving high capacitance loads. This driver is specified to drive a 4 nF capacitance with rise and fall times below 4 ns while allowing 20 A peak current. Current monitoring is provided by a 0.1 Ω shunt resistor in the OLED ground path. To further improve the dynamic response we incorporate a variable bias voltage with a programmable voltage source (Keithley SMU 238) and a bias-T into the setup. The applied offset and peak voltage are 6 V and 18 V, respectively. Fig. 8 shows a scheme of the transmission line.

Rise and fall times on the order of 30 ns were measured with an inorganic detector (Thorlabs DET10A). A maximum fibre output power of 4.4 µW could be achieved at 20 V DC. While transmitting an S/PDIF signal the OLED has a fibre-coupled mean optical power of ~ 2.5 µW. This compares to the S/PDIF output from inorganic LEDs emitting at 650 nm (~ 15µW).

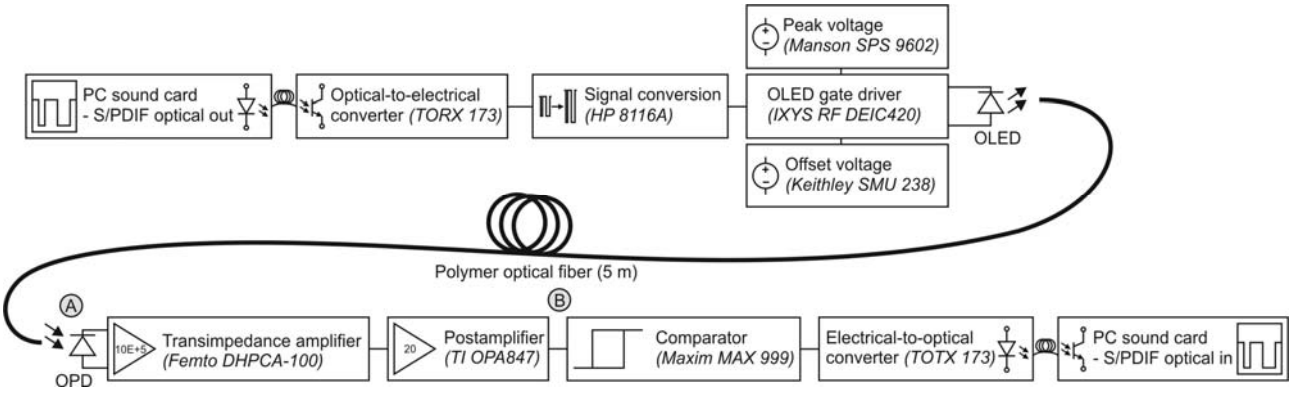


Fig. 8: Experimental setup for the S/PDIF data transmission. Digital encoded signals of a digital soundcard are amplified and applied to the OLED transmitter. The optical signal is transported through a 5-m POF and converted into electrical signals by an OPD.

To achieve a high sensitivity of the organic photodiode to the incident fibre transmitted signal a bias voltage has to be applied to the device. The OPD is connected to a transimpedance amplifier (FEMTO DHPCA-100). An ultralow noise post amplifier (Texas Instruments OPA847) amplifies the output signal of the transimpedance amplifier and adjusts the DC-offset. A high-speed comparator (Maxim MAX999) converts the resulting waveform into TTL signals which are then transmitted optically (Toshiba TOTX173) to a standard PC sound card for recording and analysis. For the measurement of eye diagrams a 1-GHz-oscilloscope (Agilent 54832D) is connected to the output of the post amplifier.

Using this setup, we were able to transmit digitally encoded audio signals at a data transfer rate of 2.8224 Mbit/s. We demonstrate a standard protocol optical data link using only organic semiconductor devices as transmitter and receiver, respectively. For an analysis of the transfer quality, we recorded eye diagrams at several points along the data transmission path using an S/PDIF transmission of white noise (44.1 kHz sampling rate). The data transfer rate is 2.8224 Mbit/s, and, therefore, the maximum theoretical eye opening is 177 ns. For the measurement of the optical signal an inorganic Si photodiode with built-in amplifier (Thorlabs PDA36A-EC) was used. Fig. 9(A) shows the eye diagram of the fibercoupled OLED signal recorded with the inorganic detector at point A in Fig. 6. This can be directly compared to Fig. 9(B) that uses the OPD as detector recorded at point B in Fig. 8.
It is visible how the OPD shows increased noise, thus decreasing the opening of the eye from 150 ns to 110 ns. After signal reconstruction from the OPD using the post amplifier and comparator a decrease of the eye opening from the initial 165 ns at the S/PDIF-output of the transmitting soundcard to 95 ns due to the increased jitter is found, but still a very low bit error rate can be expected.

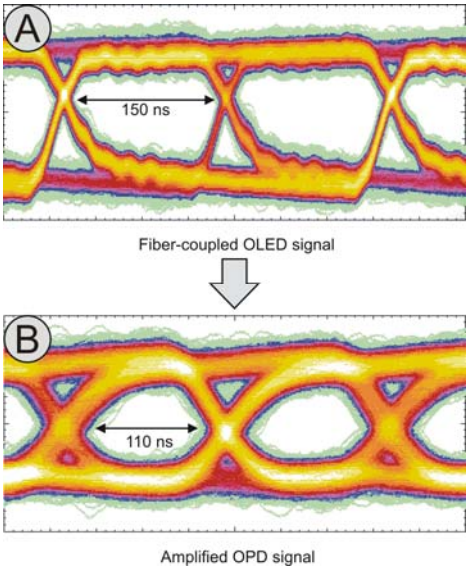


Fig. 9: Eye diagrams recorded at several points along the optical interconnect system (see Fig. 6). The original S/PDIF signal drives the OLED circuitry. The OLED signal is coupled into the POF (A) and detected and amplified by the OPD circuitry (B).

Since unencapsulated organic photodiodes are prone to degradation in ambient conditions, we investigate the transient properties during degradation under different humidity levels and with different electrode materials [A4.2:11]. The results show that encapsulation from humidity levels found in ambient air prevents degradation related to PEDOT:PSS and ITO electrode materials. For strongly improved device performance, we develop a high frequency encapsulation of organic photodiodes on a printed circuit board (PCB). This encapsulation method strongly improves lifetimes of organic photodiodes in ambient conditions [A4.2:8].

## 4. Plasmonic enhancement

For the convergence of photonics and electronics one of the main challenges is to overcome the difference in size between the micrometer scale optical and the nanometer scale electronic device. Nanoantennas are promising devices that overcome the diffraction limit and therefore the mismatch between these dimensions. In addition, the highly enhanced fields at the extremities of such structures can cause nonlinear effects and enable absorption at long wavelengths via multi-photon absorption.
A tempting possibility to further improve the above described organic photodetectors lies in the combination with different nanostructures, for example nanoantennas. By exploiting the specific antenna effects and the advantages of organic materials we want to improve the efficiency of photon detection, to tailor the device properties according to their application – for example to wavelength or polarization sensitive applications – and to shrink them in order to pave the way towards single-photon organic semiconductor devices and highly sensitive high speed photodetectors.

In order to design and to study the novel hybrid organic-nanoantenna devices, detailed scientific knowledge in the fields of organic semiconductors, antenna theory and plasmonics needs to be taken into account. The presented project highly benefits from the fact that the necessary fabrication methods are readily available and well established. The work links the activities of plasmonics and organic electronics. The combined fabrication of organic semiconductor devices with metallic nanostructures and the subsequent characterization requires a multitude of different processes.

A reliable protocol for the nanoantenna fabrication has been found and the investigation of different nanoantenna phenomena has led to several publications [A4.2:7, A4.2:10, A4.2:12]. The work is accompanied by theoretical work modeling the electromagnetic field distribution of nanoantennas. The near- and far-field properties of the antennas - dominated by localized surface plasmons - can be described via Maxwell's equations, which can be solved by different numerical methods. Here, we choose the two simulation tools, Lumerical based on the Finite Difference Time Domain (FDTD) method [40] and COMSOL Multiphysics [41] based on the Finite Element Method (FEM) for simulations.
The simulations are intended to provide a better understanding of the physical behavior of nanoantennas and their interaction with organic semiconductor materials and devices. Furthermore, such simulations help to identify an optimized antenna and device geometry.

A fundamentally different approach how organic semiconductor devices can be improved by nanostructures has been followed in parallel. Here, we investigated the incorporation of a nanoscale silver grating onto the ITO-anode of a standard organic photodiode utilizing again FDTD simulations. In contrast to the combination with nanoantennas, which focuses on the downscaling of device sizes, the use of periodic gratings is rather intended to optimize the existing relatively large scale devices. The method of plasmonic field enhancement has already been employed for the tuning of absorption properties in high-speed inorganic photodiodes [A4.2:1]. We optimized the grating structure regarding grating thickness, period and fill ratio for a wavelength of 650 nm. 650 nm is a widely used wavelength for POF optical interconnects due to a attenuation dip in PMMA fibers.
For first experiments we are fabricating silver gratings on ITO covered glass with electron beam lithography. Further device fabrication is to be done by laser interference lithography to allow the structurization of large areas. Investigation of the optoelectronic properties of these devices in an experimental setup is underway.

### 4.1 Fabrication and characterization of gold nanoantennas

We have successfully fabricated two arm and single arm gold dipole antennas (gap ~20 nm, width ~20 nm, height ~25 nm, variable arm length of 25 nm to 65 nm) using electron beam lithography in cooperation with the group of Prof. M. Siegel (Fig. 10).
A glass cover slip is covered with a 30 nm layer of indium tin oxide (ITO) that serves as a conducting layer for the electron beam step and also helps to provide improved adhesion of the gold on the surface. The electron beam resist PMMA (poly(methylmethacrylate)) is spun onto it and electron beam lithography is performed. After development a 30 nm gold layer is deposited via thermal evaporation and subsequently a lift-off process is performed resulting in gold nanoantenna structures resonant at optical frequencies.

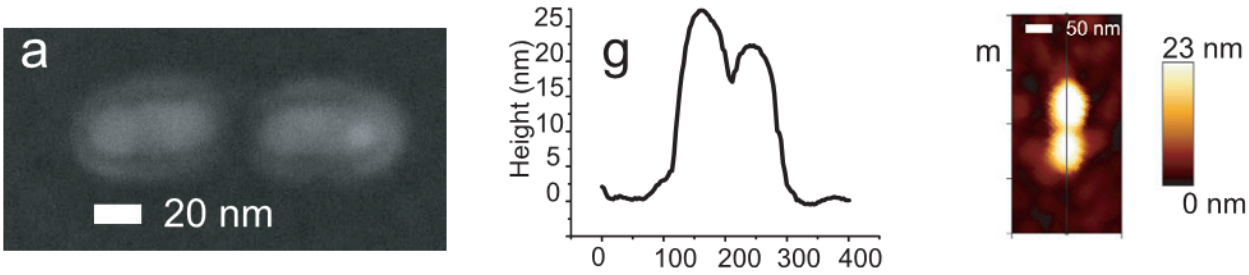


Fig. 10: Exemplary SEM and AFM image with extracted corresponding height profile of a gold dipole nanoantenna with 20 nm width, 65 nm arm length and 20 nm gap width. [A4.2:7]

The topographical properties of the structures are measured with high accuracy by means of atomic force and scanning electron microscopy. Optical measurements are performed using scattering far-field detection via dark-field microscopy. For detection either a single photon avalanche photodiode or a spectrometer with an EMCCD camera can be used.

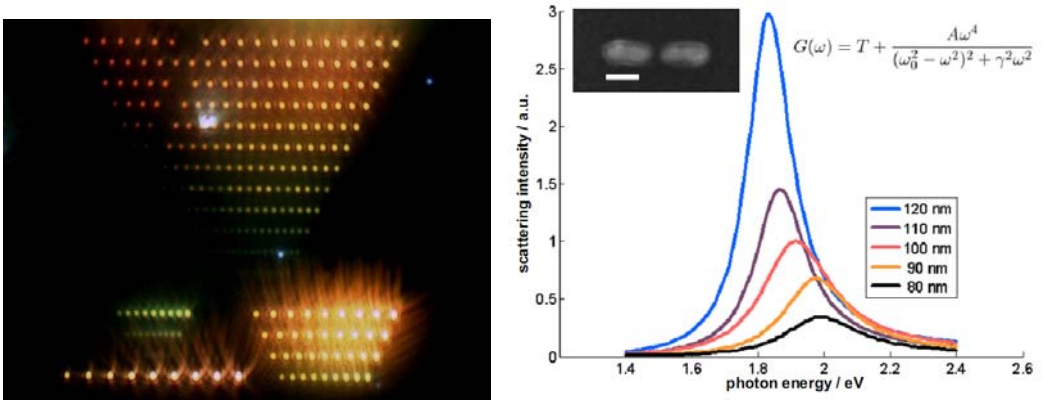


a) b)

Fig. 11: a) CCD real color image of scattering from different antennas.
b) Fitted far-field scattering spectra of two arm dipole antennas with different total antenna lengths and SEM image (see inset, scale bar 40 nm).

For coupled dipole nanoantennas, an enhanced scattering response and a shift in resonance have been measured in comparison to single gold rods. The influence of the gap size on the scattering response has also been investigated [A4.2:7]. A very high localization of electromagnetic fields has additionally been shown for single rods at their extremities [A4.2:10].

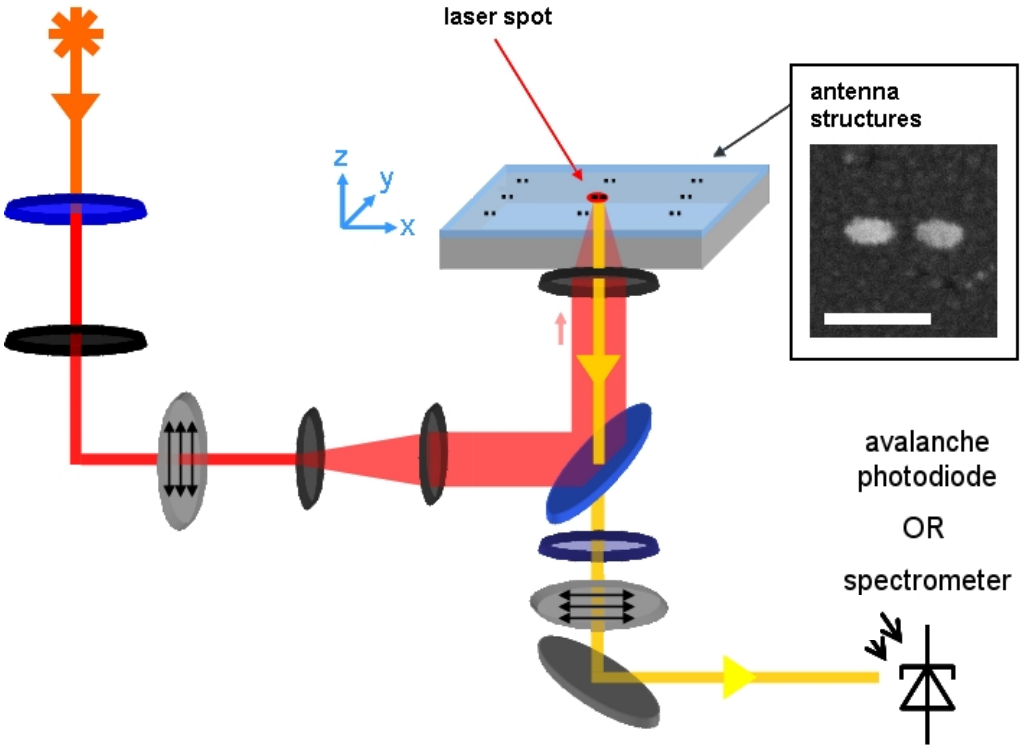


Fig. 12: Measurement setup for non-linear antenna characterization. The inset shows an SEM image of a gold dipole nanoantenna with arm lengths of 45 nm and a gap width of 20 nm (scale bar is 100 nm). [A4.2:12]

Additionally, non-linear characterization of such optical antennas has been performed, providing further insight into the mechanism of plasmon generation as well as into the radiative relaxation channels present in such nanostructures [A4.2:12]. To this end, nanostructures were excited non-resonantly using a pulsed laser operating at a constant wavelength (810 nm) and the plasmonic response was observed (Fig. 12). Such observations allow for a greater understanding of antennas and also their possible interactions with their surroundings, e.g. organic materials.

Numerical simulations help to further understand the physical properties of nanoantennas.
Therefore, pure nanoantennas surrounded by air have been investigated to obtain a better understanding of their geometry and wavelength dependent behavior and to separate the influences of the antenna itself from the influences of the surrounding material.
For all simulations presented here, nanoantennas with a constant height of 30 nm and a width of 20 nm consisting of two antenna arms separated by a 20 nm antenna gap have been investigated. The material of the antenna structures is gold, described by its dielectric function taken from Johnson and Christy [39]. All edges and corners of the nanostructures were rounded by a radius of 3 nm to avoid unrealistic singularities in the simulations.
Figure 13 shows the characteristic near field distribution of the electric field intensity (|E-field|²) and the magnetic field intensity (|H-field|²). The electric field is highly localized in the antenna gap and at the rod ends and experiences high enhancements. The magnetic field is several orders of magnitude smaller and is mainly present at the sides of the rods.

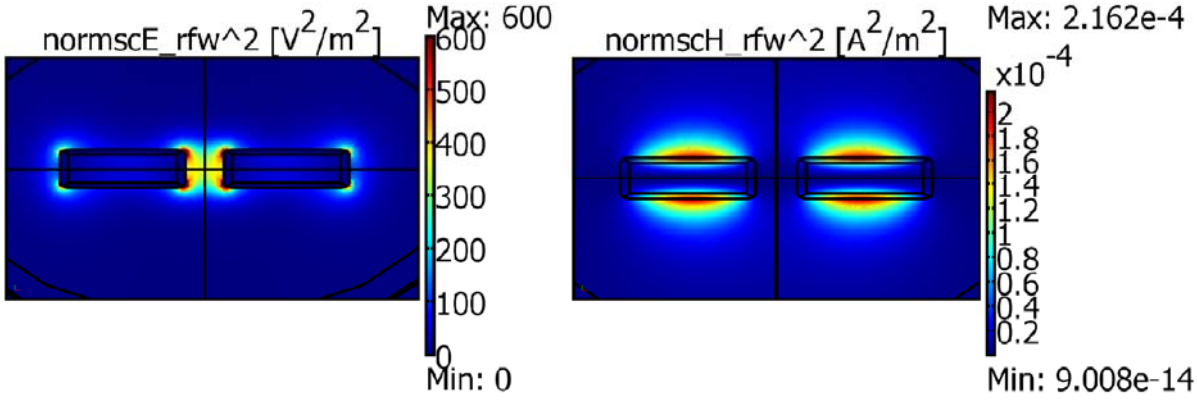


a) b)

Fig. 13: Simulation with COMSOL Multiphysics; arm length: 65 nm
a): Near-field distribution of |E-field|²;strongly enhanced field in the gap;
b) Near-field distribution of |H-field|², week magnetic fields at the sides of the antenna

Figure 14 shows three important far-field properties of such nanoantennas. The absorption cross section is proportional to the power absorbed in the nanostructure, while the scattering cross section is related to the power scattered by the antenna. As explained above, the scattering response can be measured experimentally by dark-field microscopy. The extinction cross section is the sum of the two cross sections mentioned before. As can be seen, all three have a strong resonance at the same wavelength position. This resonance wavelength depends mainly on the antenna length and the dielectric function of the metal structure and the surrounding environment.

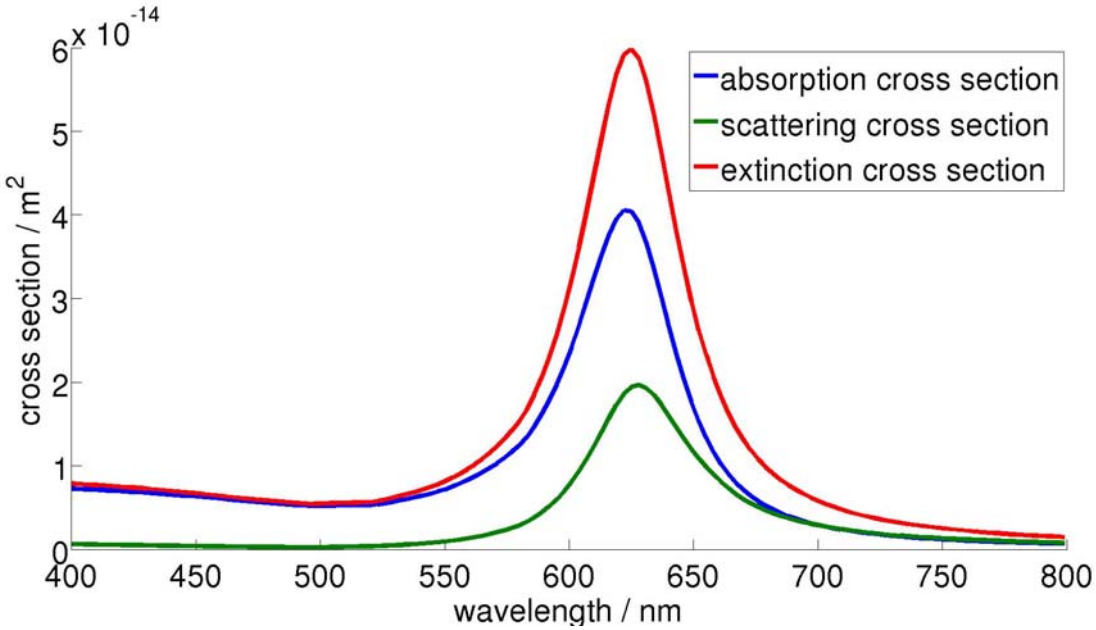


Fig. 14: Absorption, scattering and extinction cross section; arm length: 65 nm; simulation with COMSOL Multiphysics

For a better comparison with measured data, the nanoantennas of all following simulations were placed on a 30 nm ITO layer on top of a glass substrate. For the ITO layer a complex and frequency dependent refractive index was taken, the glass substrate can be described by a constant refractive index of n=1.5.

### 4.2 Concepts for nanoantenna organic optoelectronic devices

In accordance with the performed simulations and the comprehensive experimental investigations of the fabricated gold dipole antennas, an OPD consisting of a single gold dipole nanoantenna, two rectangularly shaped ITO electrodes that are aligned perpendicular to the long antenna axis, organic layers and an encapsulation layer is the most promising design for a first fabrication attempt (Fig. 15). It is an experimental challenge to combine the nanoscale and microscale dimensions of such architecture with high alignment precision.

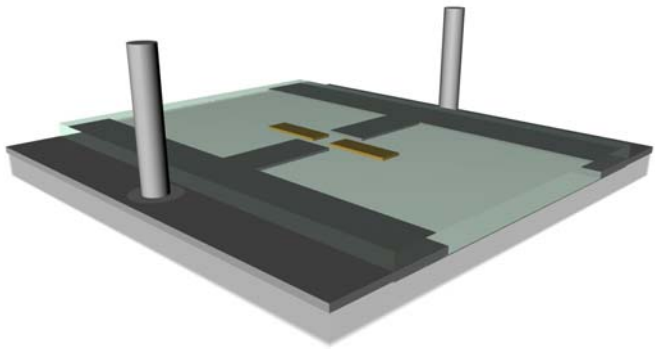

Fig. 15: Layout (not to scale) of the nanoantenna-organic photodetector device consisting of a nanoscale dipole antenna and microscale rectangularly shaped electrical contacts. The ITO electrodes and the nanoantennas are fabricated in a two-step e-beam lithography and lift-off process. Subsequently the organic layers and an encapsulation will be deposited.

The transparent sleeve electrodes (Fig. 16) will not affect the antenna properties significantly. They have to be sufficiently conducting to convert photocarriers that are generated in the tiny antenna gap into an electrical signal while being optically transparent. The thickness should be in the range of the antenna height.

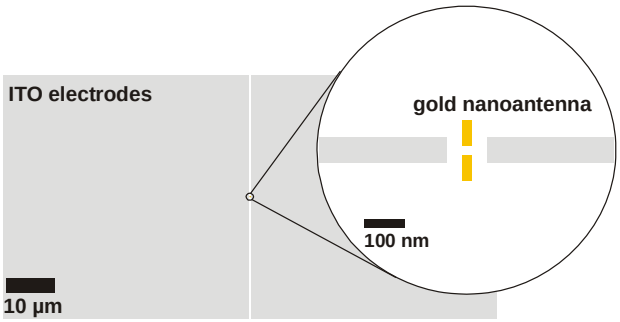


Fig. 16: Concept for the nanoantenna-organic photodetector device consisting of a nanoscale dipole antenna and microscale rectangularly shaped electrical contacts. The organic material will be deposited on top of the antenna region.

Simulations were carried out to investigate the influence of the organic layer on the antenna properties. The thickness of this additional layer was set to 60 nm.
In Figure 17 it can be seen that the resonance wavelength red-shifts significantly, when the refractive index of the covering material is increased and the resonance becomes broader. Another very interesting feature is the fact that the scattering response of a material with refractive index of n=1.7 is significantly higher than for an antenna placed in air. When increasing the refractive index further, the scattering response slowly decreases. This can be explained by the fact that a refractive index of 1.7 is very close to the refractive index of ITO. Hence, for this refractive index the nanoantenna experiences the same refractive index at all sides, which is favourable for plasmonic resonances. When the antenna is surrounded by materials with different refractive indices the resonance intensity decreases.

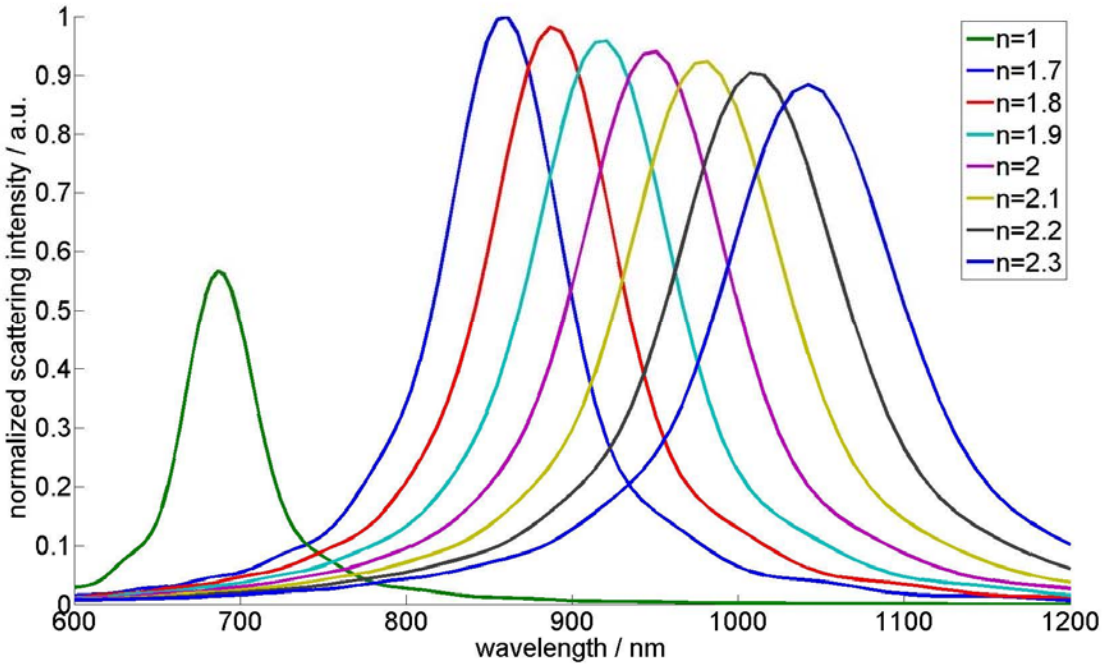


Fig. 17: Simulation with Lumerical; normalized scattering intensity for nanoantennas covered with a 60 nm layer of a dielectric material with a constant refractive index; arm length 60 nm antenna on 30 nm ITO layer on glass substrate;

Finally, simulations have been carried out where the complex and frequency dependent refractive index of P3HT:PCBM was chosen for the covering layer. The refractive index of P3HT:PCBM is around $\tilde{n} = 1.8 + j * 0.002$ in the wavelength range of 900 nm. Again, it can be seen how the resonance wavelength is red shifted and the peak is broadened. It can be seen that the real part of the resonance behaviour is mainly dominated by the real part of the refractive index at resonance and the imaginary part, which is very small, can be neglected.

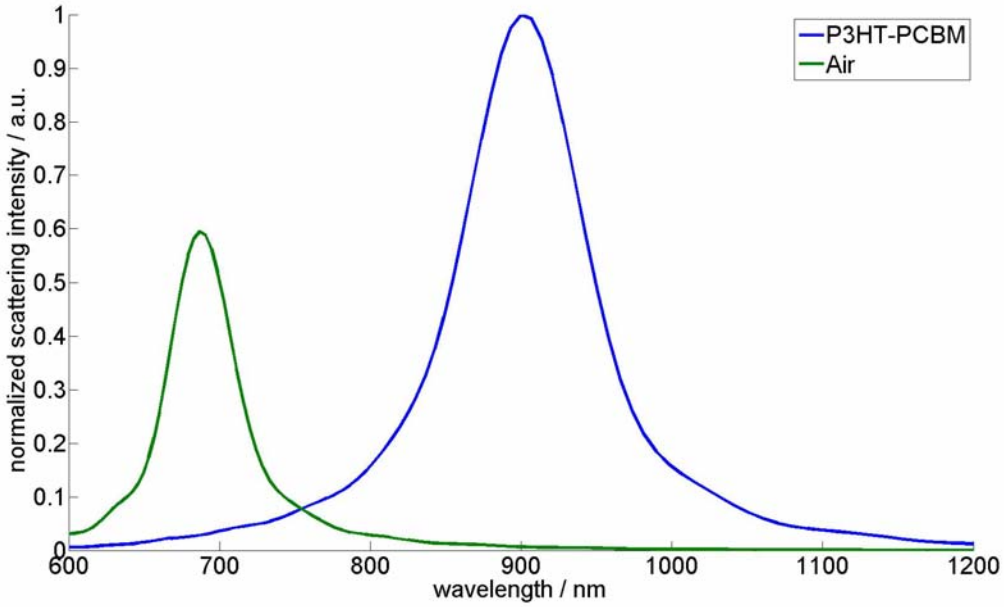


Fig. 18: Simulation with Lumerical; normalized scattering intensity; arm length: 60 nm; ITO layer thickness: 60 nm

The observed red-shift in optical resonance needs to be taken into account when planning the device layout, especially the antenna geometry.

Concerning the fabrication of the presented devices, the deposition of the thin ITO layer is performed via RF sputtering in our cleanroom as well as the deposition of the organic layers via spin-coating or thermal evaporation.

The required nanometer accuracy in the alignment of the two-step e-beam lithography process and the combination of the nanoscopic antenna and the microscopic electrical contact lengthscales lead to a challenging fabrication protocol that we are currently carrying out.

## References

*- own work with complete titles -*

[1] www.toshiba.com

[2] www.samsung.com

[3] www.konarka.com

[4] Peumans, P.; Yakimov, A.; Forrest, S. R., J. Appl. Phys. 93(7), 3693-3723 (2003).

[5] Schilinsky, P.; Waldauf, C.; Hauch, J.; Brabec, C. J., Thin Solid Films 451–452, 105-108 (2004).

[6] Hoppe, H.; Sariciftci N. S., J. Mater. Res. 19(7) 1924-1944 (2004).

[7] Brabec, C. J.; Sariciftci, N. S.; Hummelen, J. C., Adv. Func. Mat. 11(1), 15-26 (2001).

[8] B. Lamprecht, R. Thünauer, M. Ostermann, G. Jakopic, G. Leising, phys. stat. soli. 202 (5), R50-R52 (2005)

[9] Burns, M. A.; Johnson, B. N.; Brahmasandra, S. N.; Handique, K.; Webster, J. R.; Krishnan, M.; Sammarco, T. S.; Man, P. M.; Jones, D.; Heldsinger, D.; Mastrangelo, C. H.; Burke, D. T., Science 282, 484-487 (1998).

[10] Verpoorte, E., Lab Chip 3, 42N–52N (2004).

[11] Choudhury, B.; Shinar, R.; Shinar, J., J. Appl. Phys. 96(5), 2949-2954 (2004).

[12] Hofmann, O.; Wang, X.; Demello, J. C.; Bradley, D. D.; Demello, A. J., Lab Chip 5, 863-868 (2005).

[13] Yao, B.; Luo, G.; Wang, L.; Gao, Y.; Lei, G.; Ren, K.; Chen, L.; Wang, Y.; Hu, Y.; Qiu, Y., Lab chip 5, 1041-1047 (2005).

[14] A. Colsmann, F. Stenzel, G. Balthasar, H. Do, U. Lemmer, *Plasma patterning of poly(3,4-ethylenedioxythiophene):poly(styrenesulfonate) anodes for efficient polymer solar cells*, Thin Solid Films, Thin Solid Films 517, 1750 (2009).

[15] Mikkel Jørgensen, Kion Norrman and Frederik C. Krebs, Sol Mat 92 (7), 686-714 (2008).

[16] U. Geyer, J. Hauss, B. Riedel, S. Gleiss, U. Lemmer and M. Gerken, Large-scale patterning of indium tin oxide electrodes for guided mode extraction from organic light-emitting diodes, J. Appl. Phys. 104, 093111 (2008).

[17] Stroisch, M.; Woggon, T.; Lemmer, U.; Bastian, G.; Violakis, G.; Pissadakis, S., "Organic semiconductor distributed feedback laser fabricated by direct laser interference ablation," Opt. Exp. 15(7), 3968-3973 (2007).

[18] Punke, M.; Mozer, S.; Stroisch, M.; Bastian, G.; Gerken, M.; Lemmer, U.; Rabus, D.G.; Henzi, P.: *"Organic semiconductor devices for micro-optical applications,"* Proc. SPIE 6185, 618505-1-618505-13 (2006).

[19] Ohmori, Y.; Kajii, H.; Kaneko, M.; Yoshino, K.; Ozaki, M.; Fujii, A.; Hikita, M.; Takenaka, H.; Taneda, T., IEEE J. Sel. Top. Quantum Electron. 10(1), 70-78 (2004).

[20] T. Komatsu, S. Kaneko, S. Miyanishi, K. Sakanoue, K. Fujita, and T. Tsutsui, Jpn. J. Appl. Phys., vol. 43, no. 11A, pp. L1439–L1141, 2004.

[21] P. Peumans, V. Bulovic, and S. R. Forrest, Appl. Phys. Lett. 76, 3855 (2000).

[22] T. Morimune, H. Kajii, and Y. Ohmori, Jpn. J. Appl. Phys., Part 1 45, 546 (2006).

[23] G. Yu, J. Gao, J. Hummelen, F. Wudl, and A. J. Heeger, Science **270**, 1789 (1995).

[24] J. G. Müller, J. M. Lupton, J. Feldmann, U. Lemmer, M. C. Scharber, N. S. Sariciftci, C. Brabec, and U. Scherf, *Ultrafast dynamics of charge carrier photogeneration and geminate recombination in conjugated polymer:fullerene solar cells*, Phys. Rev. B **72**, 195208 (2005).

[25] V. D. Mihailetchi, H. X. Xie, B. de Boer, L. J. A. Koster, and P. W. M.Blom, Adv. Funct. Mater. **16**, 699 (2006).

[26] W. Ma, C. Yang, X. Gong, K. Lee, and A. J. Heeger, Adv. Funct. Mater.**15**, 1617 (2005).

[27] M. Reyes-Reyes, K. Kim, and D. L. Carroll, Appl. Phys. Lett. **87**, 083506 (2005).

[28] Alexander Colsmann, Johannes Junge, Thomas Wellinger, Christian Kayser and Uli Lemmer, *Optimization of electron transport and cathode materials for efficient organic solar cells*, Proc. of SPIE **6192**, 619220-1 (2006).

[29] A. Colsmann, J. Junge, C. Kayser, U. Lemmer, *Organic tandem solar cells comprising polymer and small-molecule subcells*, Appl. Phys. Lett. **89**, 203506 (2006).

[30] Gärtner, C.; Karnutsch, C.; Pflumm, C.; Lemmer, U.: *"Numerical Device Simulation of Double Heterostructure Organic Laser Diodes Including Current Induced Absorption Processes,"* IEEE J. Quantum Electron. 43(11), 1006-1017 (2007).

[31] C. Gärtner, C. Pflumm, C. Karnutsch, V. Haug, U. Lemmer, *"Numerical study of annihilation processes in electrically pumped organic semiconductor laser diodes"*, Proceedings of the SPIE: Organic Light-Emitting Materials and Devices X, 63331J (2006).

[32] C. Gärtner, C. Karnutsch, C. Pflumm, U. Lemmer, "*The Influence of Annihilation Processes on the Threshold Current Density of Organic Laser Diodes*", Journal of Applied Physics 101, 023107 (2007).

[33] C. Berger, M. A. Kossel, C. Menolfi, T. Morf, T. Toifl, and M. L. Schmatz. Proc. SPIE, vol. **4942**, pp. 222–235, 2003.

[34] C. Thiel and R. König, in Proc. VDI Berichte, vol. 1415, pp. 819-834, 1998.

[35] D. A. B. Miller, Int. J. Optoelectron., vol. 11, No. 3, pp. 155-168, 1997.

[36] H. Cho, P. Kapur, and K.C. Saraswat, *J. Lightw. Technol.*, vol. 22, no. 9, pp. 2121–2133, Sep. 2004.

[37] B. Wittmann, M. Jöhnck, A. Neyer, F. Mederer, R. King, and R. Michalzik, *IEEE J. Sel. Topics Quant. Electron.*, vol. 5, no. 5, pp. 1243–1248, Sep. 1999.

[38] Toslink Optical Fiber Connection System, [Online]. Available: http://www.toshiba.com

[39] P.B. Johnson and R.W. Christy. Optical constants of noble metals. Phys. Rev. B, 6:4370–4379, 1972.

[40] Lumerical FDTD Solution, http://www.lumerical.com/.

[41] COMSOL Multiphysics, http://www.comsol.com